Journal of Power Sources 493 (2021) 229691

Contents lists available at ScienceDirect

Journal of Power Sources

journal homepage: www.elsevier.com/locate/jpowsour

Enhanced proton conductivity and stability of Ba-deficient $BaCe_{0.8}Y_{0.2}O_{3-\delta}$

Ángel Triviño-Peláez [a], Domingo Pérez-Coll [a], Jadra Mosa [a], Clemens Ritter [b], Ulises Amador [c], Glenn C. Mather [a,*]

[a] Instituto de Cerámica y Vidrio (CSIC), Campus de Cantoblanco, 28049, Madrid, Spain
[b] Institut Laue Langevin, 71 Avenue des Martyrs, Grenoble, 38042, France
[c] Departamento de Química, Facultad de Farmacia, Universidad CEU-San Pablo, Boadilla del Monte, 28668, Madrid, Spain

HIGHLIGHTS

- $Ba_{0.95}Ce_{0.8}Y_{0.2}O_{3-\delta}$ crystallises with monoclinic distorsion of pervoskite structure
- Ba deficiency promotes resistance to carbonation in $BaCe_{0.8}Y_{0.2}O_{3-\delta}$
- H^+ conductivity dominates in wet conditions and is greater for Ba-deficient phase

GRAPHICAL ABSTRACT

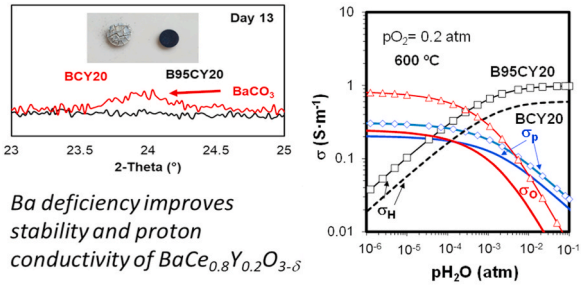

ARTICLE INFO

Keywords:
A-site substoichiometry
Proton transport
Partial conductivity
Protonic ceramic fuel cell
BCY
Barium cerate

ABSTRACT

A-cation deficiency has a significant impact on the properties of proton-conducting perovskites (ABO_3), depending on factors such as the ionic radius, concentration of dopant and degree of substoichiometry of the A-site cation. Here, we focus on the influence of Ba deficiency on the structure, stability and partial electrical conductivities of the perovskite $BaCe_{0.8}Y_{0.2}O_{3-\delta}$ (BCY20). Neutron powder diffraction is employed to determine a monoclinic symmetry (space group I2/m) for $Ba_{0.95}Ce_{0.8}Y_{0.2}O_{3-\delta}$ (B95CY20), with greater distortion and specific free volume than BCY20. Confocal Raman microscopy integrated with atomic force microscopy and X-ray diffraction confirm improved resistance to carbonate formation in the Ba-deficient material. Electrical conductivity is also greater for B95CY20 in both wet and dry oxidising and moderate reducing conditions, reaching ≈1.4 and 1 S m^{-1} in dry conditions of O_2 and N_2, respectively, at 600 °C. Partial conductivities determined by a defect-chemistry-based method indicate that proton conductivity is dominant in wet air for temperatures <700 °C and greater for B95CY20 (≈0.95 S m^{-1} at 600 °C) in comparison to BCY20 (≈0.58 S m^{-1} at 600 °C), with an associated hydration enthalpy of −128 kJ mol^{-1}. Mixed oxide ionic-electronic conductivity dominates in dry oxidising conditions and, again, is greater for Ba substoichiometric material.

1. Introduction

Barium cerate perovskites ($BaCeO_3$) doped with lower valence cations on the Ce site are excellent high-temperature proton conductors with potential as membranes in applications such as electrochemical hydrogen pumps and reactors for purifying hydrogen [1], protonic

* Corresponding author.
E-mail address: mather@icv.csic.es (G.C. Mather).

https://doi.org/10.1016/j.jpowsour.2021.229691
Received 7 November 2020; Received in revised form 29 January 2021; Accepted 20 February 2021
Available online 4 March 2021

ceramic fuel cells (PCFCs) and protonic ceramic electrolyser cells (PCECs) [2–4]. However, the high basicity of the anionic network leads to poor stability of barium cerates in acidic gases such as CO_2 and high water-vapour partial pressures with decomposition to $BaCO_3$ and $Ba(OH)_2$, respectively, hindering their use in these applications [3,5–7]. Alternative strategies which find a compromise between good protonic conductivity and chemical stability have, thus, found favour in recent years. One of the more common approaches is Zr doping in solid solutions such as $BaCe_{0.9-x}Zr_xY_{0.1}O_{3-\delta}$ [8,9], although gains in stability are offset by both poorer sinterability and proton conductivity [10]. Another strategy to enhance the stability of barium cerates consists of the partial substitution of O^{2-} for F^-, Cl^- and Br^- to diminish lattice basicity [11–14]. Recent work in our group [15] indicates that synthesis of $BaCe_{0.8}Y_{0.2}O_{3-\delta}$ (BCY20) with Br by means of the Pechini method results in almost complete evaporation of the halide on high-temperature sintering to 1500 °C. However, structural and electrical properties are significantly affected by the addition of Br in the starting reactants which are *a priori* attributable to stoichiometry differences with the parent phase. BCY20 synthesized with Br exhibited poorer stability in CO_2 in comparison to the BCY20 parent material; however, total conductivity and partial proton conductivity was higher than BCY20, which was tentatively attributed to barium deficiency in the structure, likely resulting in minor Ba segregation at grain boundaries.

This interesting result follows on from recent work in which Kim et al. [16] showed that Ba-deficient $BaCeO_3$ exhibits improved grain-boundary conductivity due to the absence of a nanoscale amorphous layer at the grain boundary. The nanolayer is a preferential path for CO_2 or H_2O to react and form the carbonate or hydroxide so its removal on introducing Ba deficiency also improves stability considerably. A reassessment of the potential of barium cerate, with substoichiometric Ba content, for adoption in electrochemical devices is, therefore, warranted.

There are reports of different effects of A-site deficiency on the electrical properties of proton-conducting perovskites, with some authors indicating that the total conductivity diminishes as A-site content decreases due to a smaller lattice volume [17,18]. Nevertheless, detailed analysis of the electrical properties including determination of partial conductivities is not widely conducted and the effects of A-site deficiency on different electrical components in relevant conditions is of critical importance for tailoring compositions for use in electrochemical applications.

In this work, we prepare $Ba_{0.95}Ce_{0.8}Y_{0.2}O_{3-\delta}$ (B95CY20) by the Pechini method and compare the effects of Ba deficiency with respect to the Ba stoichiometric phase in terms of electrical properties and stability. In addition to Raman and XRD studies of the development of degradation products, particular emphasis is given to the determination of electrical-transport behaviour for protons, oxide-ions and electron holes in the temperature range 600–900 °C on suitable fitting of conductivity data in a range of oxygen and water-vapour partial pressures.

2. Experimental

A sol-gel based Pechini process was used to synthesize compositions in the $Ba_{1-x}Ce_{0.8}Y_{0.2}O_{3-\delta}$ series with nominal stoichiometric and substoichiometric amounts of barium (x = 0, labelled as BCY20; x = 0.05, labelled as B95CY20); a list identifying abbreviations and symbols used in the text is provided in Table 1. Nitrate precursors of the three cations were used as starting materials, with the water content determined by thermogravimetry in air employing an SDT Q600 instrument. The nitrates were dissolved in deionised water at ~50 °C on a hotplate while stirring continuously until complete dissolution was achieved. Citric acid and ethylene glycol were then added in excess with respect to the final product (10:1 and 40:1 M ratios, respectively) to initiate polymerization, and stirred for 30 min. The temperature of the solution was then raised in the range 60–80 °C and maintained for ~2 h, before heating at ~100 °C for more than 12 h to obtain a dark-brown polymerised complex. Organics were largely removed in two pyrolysis steps at 350 °C and 600 °C, each of 4 h in duration, with grinding in an agate mortar with acetone after each stage. The powders were then treated at 1100 °C for 4 h in order to eliminate any remaining organic product before grinding in a ball mill and sieving (100 μm). Cylindrical pellets were shaped by uniaxial pressing of the resulting powders with 37.5 MPa of pressure then sintered at 1500 °C for 4 h. Density was calculated from the geometric dimensions and mass of the samples; relative density was determined as a percentage of the crystallographic density.

Table 1
List of most relevant symbols and notations employed in the text.

Symbol/notation	Identification
BCY20	$BaCe_{0.8}Y_{0.2}O_{3-\delta}$
B95CY20	$Ba_{0.95}Ce_{0.8}Y_{0.2}O_{3-\delta}$
pO_2, pH_2O	oxygen partial pressure, hydrogen partial pressure
K_w	equilibrium constant of hydration reaction
K_o	equilibrium constant of oxidation reaction
Y'_{Ce}, Y_{Ba}	yttrium species at cerium and barium positions
$v'''_{Ce}, v''_{Ba}, v^{\cdot\cdot}_O$	cerium-vacancy, barium-vacancy and oxygen-vacancy species
$h^{\cdot}$, $OH_O^{\cdot}$	electron-hole and protonic species
α	defined constant according to eq. (11)
σ_T	total conductivity
σ_H, σ_O, σ_p	protonic, oxide-ionic and electron-hole conductivities
σ_H^0	protonic conductivity at $pH_2O = 1$ atm
σ_O^0	oxide-ionic conductivity at $pH_2O = 0$ atm
σ_p^0	electron-hole conductivity at $pH_2O = 0$ atm and $pO_2 = 1$ atm
t_H, t_O, t_p	protonic, oxide-ionic and electron-hole transport numbers

Completeness of reaction and phase purity were evaluated by powder X-ray diffraction (XRD) on a Bruker D8 high-resolution diffractometer, with monochromatic Cu($K\alpha_1$) radiation (λ = 1.5406 Å) obtained employing a germanium monochromator. Samples were prepared for XRD analysis by lightly polishing the external faces of sintered pellets to remove any surface impurities before grinding to a fine powder. Neutron powder diffraction (NPD) of milled B95CY20 was performed at room temperature on the high resolution D2B diffractometer at the Institut Laue Langevin, selecting a monochromatic beam wavelength of 1.594 Å from the primary beam with a Ge monochromator. The Fullprof software [19] was used to perform Rietveld refinement of the NPD data.

Electrodes for electrical measurements were prepared on coating polished pellet surfaces with Pt paste (Heraeus CL11-5349) followed by firing at 950 °C for 1 h. Impedance spectroscopy was performed in potentiostatic mode with an Autolab PGStat302N-FRA2 instrument working in the frequency range $0.1 \leq f \leq 10^6$ Hz with a signal amplitude of 50 mV. Electronic mass-flow controllers (Bronkhorst) of O_2 and N_2 provided gas flows to a single-cell measuring chamber with measurements registered on cooling in the temperature range 400–900 °C in steps of 50 °C. Dry atmospheres were achieved on flowing the gases through a drying column with a packed bed of commercial aluminosilicate and zeolite beads (Supelco); wet conditions ($pH_2O \approx 0.022$ atm) were obtained on bubbling gases through KBr-saturated H_2O at room temperature.

Impedance spectroscopy was also employed to measure the pO_2-dependence of total conductivity in isothermal conditions at different humidifications and thereby determine partial protonic, oxide-ionic and electronic conductivities, employing a method described previously [15,20]. Discrete oxygen partial pressures in different conditions of pH_2O were obtained on mixing wet and dry O_2 and N_2 gas flows in different ratios. Impedance measurements were registered in the ranges $10^{-4} \leq pO_2 \leq 1$ atm and $1.2 \times 10^{-3} \leq pH_2O \leq 2.2 \times 10^{-2}$ atm in a temperature interval of 600–900 °C. Experimental values of pO_2 for different gas conditions were registered by means of a YSZ sensor located adjacent to the sample.

Impedance spectra were fitted employing appropriate equivalent

circuits to determine bulk, grain-boundary and electrode contributions to the impedance response in accordance with their expected capacitance values [21] with the Zview 2.9c program (Scribner Associates).

To assess degradation related to the formation of carbonate or hydroxide species, a number of cylindrical pellets of x = 0 and 0.05 of the $Ba_{1-x}Ce_{0.8}Y_{0.2}O_{3-\delta}$ series, previously sintered at 1500 °C for 4 h, were exposed to laboratory air at room temperature for up to 13 days. During this period, the laboratory air temperature was in the range ~20–23 °C and relative humidity of the outside air was in the range 35–83%. Samples were ground approximately every 48 h then analysed by X-ray diffraction (Bruker D8 diffractometer) and Raman spectroscopy; samples were either analysed immediately or maintained in a glove box under argon prior to analysis. A stability analysis was also performed by impedance spectroscopy in air at 700 °C, before and after exposure to a 10%CO_2:90%Ar atmosphere for 168 h. Conductivity was further measured at 600 °C over a period of 72 h in flowing wet 10%H_2:90%N_2 to assess stability in reducing conditions, following a stabilisation period in the same conditions for 24 h.

Raman spectra were recorded using confocal Raman microscopy (CRM) integrated with atomic force microscopy (AFM) on a CRM-Alpha 300 RA microscope (WITec, Ulm, Germany) equipped with a Nd:YAG dye laser operating at 532 nm and a 100 objective lens (NA ¼ 0.9). The incident laser power was 5 mW and the Raman spectral resolution was down to 0.02 cm^{-1}. The sample was mounted on a piezo-driven scan platform with 4 nm lateral and 0.5 mm vertical positional accuracy. The piezoelectric scanning table allows steps of 3 nm (0.3 nm in the vertical direction), giving a very high spatial resolution for both AFM and CRM. The superficial XY areas selected for study were 30 μm × 30 μm, with an acquisition time of 0.05 s for a single spectrum. Collected spectra were analysed using Witec Control Plus software.

3. Results

3.1. Phase analysis and structure

The XRD powder pattern of $Ba_{0.95}Ce_{0.8}Y_{0.2}O_{3-\delta}$ (B95CY20) indicated a phase-pure distorted perovskite structure. NPD was subsequently employed for the determination of space group since minor distortion of the perovskite structure resulting from tilting of the BO_6 octahedra are more easily detected by neutron diffraction due to the higher scattering length of oxygen to neutrons in comparison to X-rays. Minor amounts of second phase could be discerned in the neutron pattern but could not be readily identified. Rietveld refinement proceeded in space group I2/m in accordance with both the neutron refinement of Malavasi of BCY20 [22] and our recent report of BCY20 and Br-synthesized BCY20 [15]; higher symmetry space groups, e.g. Pnma, gave poorer refinements or could be readily discounted. Oxygen occupancies were fixed at full occupancy except for the O2 site which was found to accommodate a very small amount of vacancies; nevertheless, the oxygen content refined to almost full occupancy indicating close to complete hydration, as observed for similar systems at room temperature [23], in accordance with the following hydration equilibrium:

$$H_2O + O_o^x + v_o^{\cdot\cdot} \overset{K_W}{\leftrightarrow} 2OH_o^{\cdot};\ \ K_W \approx \frac{\left[OH_o^{\cdot}\right]^2}{\left[v_o^{\cdot\cdot}\right] pH_2O} \quad (1)$$

A-site deficiency is generally compensated in perovskite systems, such as $Ba_{0.95}Ce_{0.8}Y_{0.2}O_{3-\delta}$, either by the formation of A-site vacancies

$$0.95BaO + 0.8CeO_2 + 0.1Y_2O_3 \rightarrow 0.95Ba_{Ba}^{\times} + 0.8Ce_{Ce}^{x} + 0.2Y_{Ce}^{'} + \\ +2.85O_O^x + 0.05v_{Ba}^{''} + 0.15v_O^{\cdot\cdot} \quad (2)$$

or by partitioning of the dopant cation on both A and B sites [24].

$$0.95BaO + 0.8CeO_2 + 0.1Y_2O_3 \rightarrow 0.95Ba_{Ba}^{\times} + 0.025Y_{Ba}^{\cdot} + 0.8Ce_{Ce}^{x} + 0.175Y_{Ce}^{'} + \\ +2.85O_O^x + 0.075v_O^{\cdot\cdot} \quad (3)$$

where the following consideration was applied:

$$0.025v_{Ba}^{''} + 0.025v_{Ce}^{''''} + 0.075v_O^{\cdot\cdot} \rightarrow null \quad (4)$$

Note that the second term of eq. (3) may be rewritten as a perovskite with full cation occupancy as follows:

$$\frac{0.95}{0.975}Ba_{Ba}^{\times} + \frac{0.025}{0.975}Y_{Ba}^{\cdot} + \frac{0.80}{0.975}Ce_{Ce}^{x} + \frac{0.175}{0.975}Y_{Ce}^{'} + \frac{2.85}{0.975}O_O^x + \frac{0.075}{0.975}v_O^{\cdot\cdot} = \\ = 0.9744Ba_{Ba}^{\times} + 0.0256Y_{Ba}^{\cdot} + 0.8205Ce_{Ce}^{x} + 0.1795Y_{Ce}^{'} + 2.9231O_O^x + 0.0769v_O^{\cdot\cdot} \quad (5)$$

The defect reactions (2) and (3) create and consume oxygen vacancies, respectively. Refinements were performed according to both mechanisms, restraining the cation occupancies and thermal vibration parameters for the sake of comparison due to the tendency for these factors to correlate [24].

Under these conditions, there was no clear preference for a particular mechanism with dopant partitioning resulting in marginally better quality criteria than the vacancy mechanism (vacancy mechanism: R_p = 1.77, R_B = 4.80%; dopant-partition mechanism: R_p = 1.75, R_B = 4.62%). Nevertheless, A-O bond length, specific free volume and defect-chemistry considerations (discussed later) compared with BCY20 indicated that A-site vacancy formation may be the more likely compensation mechanism in this case. The observed neutron diffraction pattern of B95CY20 and the difference between observed and calculated patterns for the vacancy-mechanism refinement are shown in Fig. 1(a); selected structural parameters and agreement factors are listed in Table 2.

Raman spectroscopy was also employed to analyse the structural features. The vibrations in ABO_3 perovskites correspond to A-BO_6, where a BO_6 octahedron can be considered as a single atom located at the B site, B–O stretches and O–B–O bends (A = Ba, B = Ce or Y). The Raman spectra (Fig. 1(b)) of BCY20 and B95CY20 correspond with the spectrum of barium cerate [26] and exhibit bands at frequencies of 110, 218, 360, 438 and 640 cm^{-1}. The substitution of yttrium for cerium on the B site lowers the average mass of the B site and shifts all bands to higher frequency than in $BaCe_{0.95}Y_{0.05}O_{3-\delta}$ [27] and the Y-free phase [25,26]. The low-frequency region of the spectra exhibit an out-of-plane bending mode (5B3g) dominated by barium, as well as bending vibrational modes of the $(Ce/Y)O_6$ octahedra. The strong low-frequency bands at 110 cm^{-1} for BCY20 are shifted to slightly higher frequency number for B95CY20 (113 cm^{-1}), most probably due to the greater distortion from the perovskite aristotype of the latter phase compared to the Ba stoichiometric analogue, as indicated by the results of Rietveld refinement. The bands in the wavenumber range 210–250 cm^{-1} are assigned to the bending modes of the CeO_6 octahedra and modes involving Ba^{2+} and Y^{3+} ion motions. The bands in the frequency range 300–375 cm^{-1} are characteristic of the stretching vibrational mode of CeO_6 octahedra in the perovskite structure [27,28], and are present at higher Raman shift compared with $BaCeO_3$, indicating the influence of Y^{3+} ions on the B site; the bands at 438 and 640 cm^{-1} are attributable to Ce/Y–O symmetric stretching vibrations [29].

3.2. Phase stability

The carbonation of barium cerates and zirconates is more favourable at low temperatures [30,31]. Hence, to provide a comparison of the different stabilities of Ba-stoichiometric and Ba-deficient phases, formation of carbonate (and hydroxide) was evaluated on exposure to laboratory air at room temperature. Fig. 2 shows a panel of photographic and X-ray comparisons of the x = 0 (BCY20) and 0.05 (B95CY20) phases on initial sintering at 1500 °C followed by exposure to air for up to 13 days. Relative density of the pellets was determined to be over 98% at this sintering temperature.

Visual inspection of the photographic images clearly shows the development of degradation of the Ba stoichiometric phase, with whitening of the pellet surface apparent after 6 days and cracking and

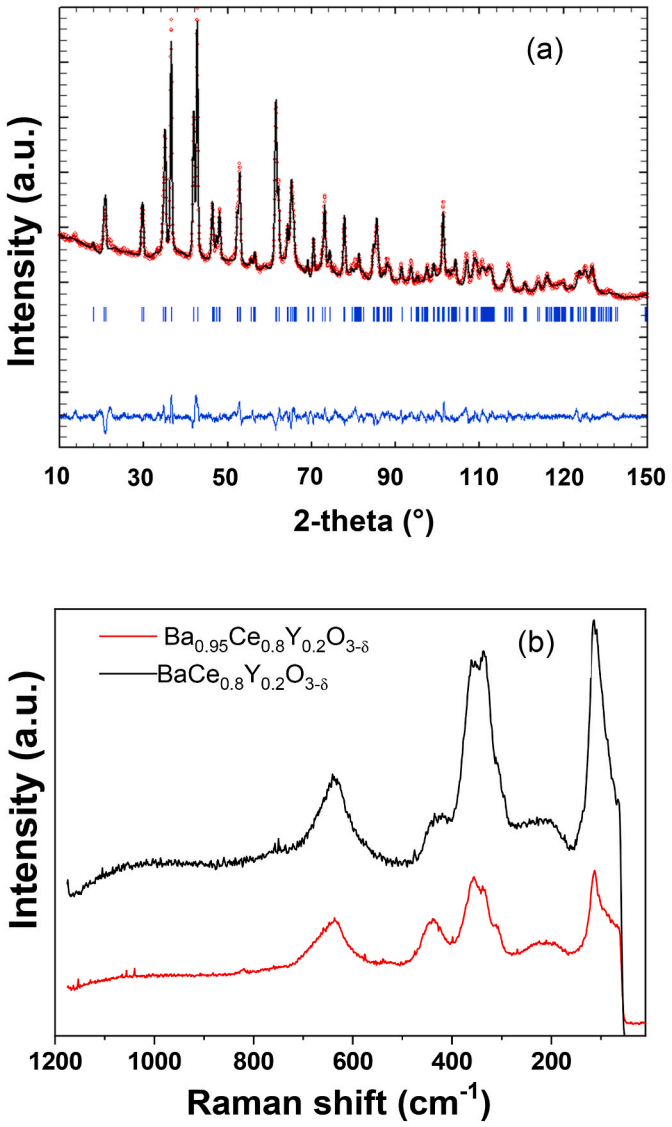

Fig. 1. (a) Experimental (red points), calculated (solid black line) and difference (blue line at bottom) NPD patterns of $Ba_{0.95}Ce_{0.8}Y_{0.2}O_{3-\delta}$ at room temperature; the vertical bars indicate the position of Bragg peaks in space group I2/m. (b) Raman spectra of BCY20 and B95CY20. (For interpretation of the references to colour in this figure legend, the reader is referred to the Web version of this article.)

spontaneous mechanical breakdown occurring thereafter. In contrast, the Ba-deficient phase maintains the same exterior aspect and good mechanical integrity throughout the 13-day period. The corresponding X-ray profiles are expanded in the 2θ range 23–25° to highlight the most intense $BaCO_3$ and $Ba(OH)_2$ reflections. It is notable that the formation of $BaCO_3$ is only clearly discerned by XRD in BCY20 after 13 days when, visually, considerable reaction appears to have occurred. The amorphous nature of the carbonate reaction product may partially explain the broad, low intensity of the $BaCO_3$ peak at 24° 2θ. It is further apparent, however, that very little carbonation is required for mechanical breakdown of the sintered bodies. This is consistent with the recent report of the formation of an amorphous nanoscale phase at the grain boundaries of barium cerate perovskites which contributes significantly to the poor stability of these phases towards carbonation [16]. We note that this reflection corresponding to carbonation is not discernible in B95CY20.

The stability of the Ba-deficient phase with respect to that of BCY20 was further confirmed by Raman spectroscopy. The extent of the surface modification as a result of carbonation after 13 days of air exposure was

Table 2
Structural parameters, interatomic distances and agreement factors for Ba95CY20 obtained from NPD at RT.

a (Å)	6.2297(6)
b (Å)	8.7346(8)
c (Å)	6.2462(7)
β (deg)	91.064(6)
V(Å^3)	339.82(6)
Ba	4i
X	0.257(1)
Z	0.767(2)
Occ	0.95
U_{iso} × 100 (Å^2)	0.5
Ce/Y	4e
Occ	0.8/0.2
U_{iso} × 100 (Å^2)	0.5
O(1)	4i
X	0.255(1)
Z	0.175(1)
Occ	1.0
U_{iso} × 100 (Å^2)	2.9(2)
O(2)	4g
Y	0.3084(7)
Occ	0.99(1)
U_{iso} × 100 (Å^2)	1.3(1)
O(3)	4h
Y	0.2770(8)
Occ	1.0
U_{iso} × 100 (Å^2)	2.7(1)

Sp. gp. *I*2/*m*, (# 12): 4i (x,0,z), 4e (¼,¼,¼), 4g (0,y,0), 4h (½,y,0).
$R_{exp} = 1.02\%$, $R_p = 1.77\%$, $R_{wp} = 2.37\%$, $R_B = 4.80\%$; $\chi^2 = 5.39$.
$\rho_{(cryst)}$: 6.03 g/cm.^{3}.

followed by means of XY Raman imaging coupled with AFM on an area of 30 μm × 30 μm, Fig. 3 (a) and (b). The regions of the Raman image are colour-coded and correspond to the Raman spectra presented in Fig. 3 (c). Two main spectra can be integrated, constructed by mapping the intensity of the 354 cm^{-1} isolated band of the BCY20 perovskite (blue spectrum in Fig. 3(c)) and the 1059 cm^{-1} band of the carbonate phase (red). The Raman images clearly confirm that 13 days of exposure of the BCY20 pellet to laboratory air results in significant formation of carbonate phase on the pellet surface (red colour). A BCY20 average spectrum after 13 days of air exposure is also plotted for comparison (black) indicating the high contribution of carbonate phase (red spectra) in the average spectra. An analogous study performed on a B95CY20 sintered pellet (green spectra) did not reveal any degradation or carbonate formation after the same period of exposure. As a further demonstration of stability of the B95CY20 phase, the electrical conductivity in air at 700 °C for B95CY20 measured before and after exposure to a CO_2 atmosphere (700 °C, 168 h), shown as a percentage loss with respect to the initial conductivity, Fig. 3(d), confirmed that negligible degradation of the electrical properties occurred during this period; the XRD pattern of B95CY20 after exposure to CO_2 is shown in Fig. S1.

As a test of stability in reducing conditions, conductivity measurements of BCY20 and B95CY20 were registered on exposure of samples to wet 10% H_2: 90% N_2 at 600 °C for 70 h after an initial period of stabilisation for 24 h in the same conditions. The conductivity of BCY20 stabilised to a steady value after around 30 h from the start of measurement (Fig. S2(a)); however, the sample degraded significantly after a period of 70 h, which was confirmed visually on its removal from the measuring set-up. The XRD pattern post-operation indicated mostly perovskite phase, but a contribution from an amorphous phase is evident (Fig. S2(c)). In contrast, the conductivity of B95CY20 remained mainly stable throughout the measured period, increasing slightly over time

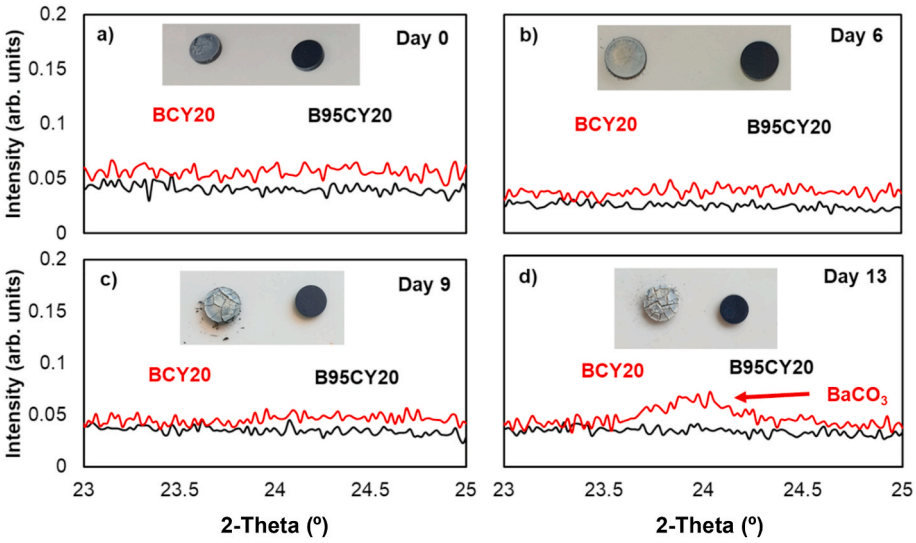

Fig. 2. XRD patterns of milled pellets and corresponding photographic images of pellet surfaces of BCY20 and B95CY20 on exposure to laboratory air for (a) 0, (b) 6, (c) 9 and (d) 13 days.

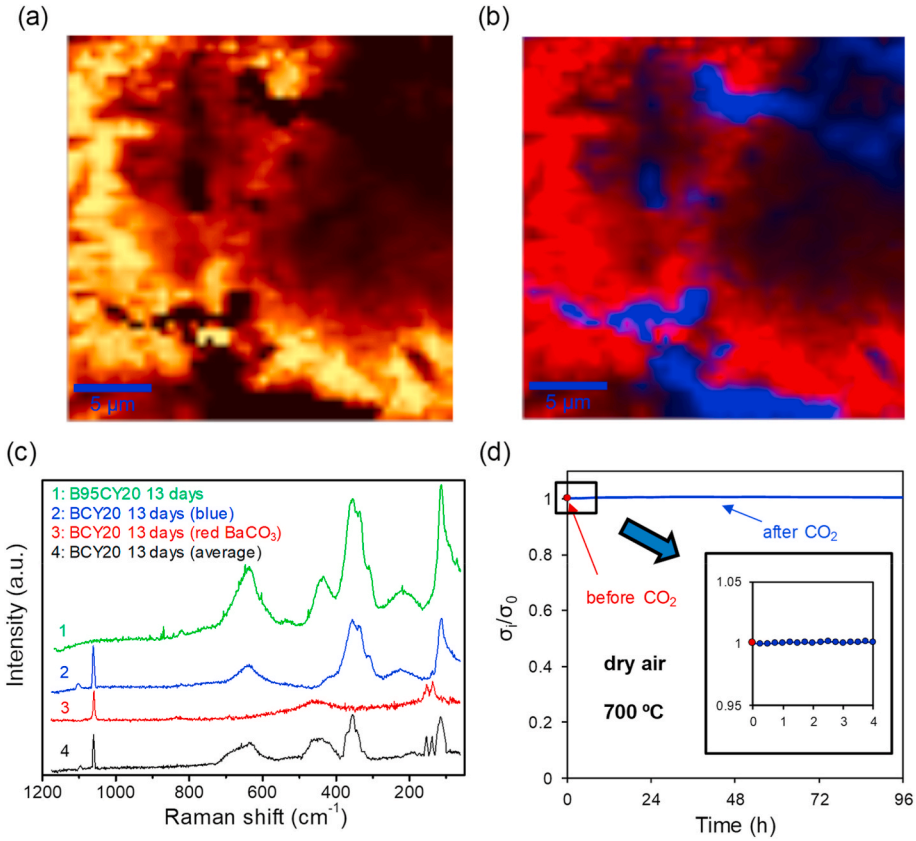

Fig. 3. Surface area (a) AFM image and (b) Raman image for XY mapping of BCY20 after 13 days of exposure to air; the red and blue areas correspond to Raman shifts of the 1059 cm^{-1} band of the carbonate impurity and the 354 cm^{-1} band of BCY20, respectively; (c) Raman spectra for the blue and red regions indicated in (b), and the average spectra of BCY20 (black) and B95CY20 (green) after 13 days exposure to air; (d) fraction of the initial conductivity of B95CY20 at 700 °C shown as a function of time, after exposure of sample to CO_2 for 168 h then reintroduction to an air atmosphere (the initial point in red indicates conductivity prior to exposure to CO_2). (For interpretation of the references to colour in this figure legend, the reader is referred to the Web version of this article.)

(Fig. S2(b)). Pellet integrity was maintained on removal from the set-up; the corresponding post-operation XRD is shown in Fig. S2(d).

3.3. Total conductivity

Fig. 4(a) shows the Arrhenius representation of total conductivity of B95CY20 in wet and dry conditions of N_2. It is apparent that the material exhibits slightly greater conductivity in dry in comparison to wet conditions in the higher temperature interval, whereas the conductivity is lower in dry in comparison to wet conditions in the lower temperature range. This change of trend between the high- and low-temperature ranges is associated with different influences of the electrical transport species as temperature is modified in wet and dry, as observed previously for barium-cerate-based materials [15].

The higher conductivity in dry in comparison to wet conditions in the high-temperature range suggests a greater dominance of electron holes, which may be depleted by water absorption in wet conditions. On the other hand, the higher conductivity in wet in comparison to dry

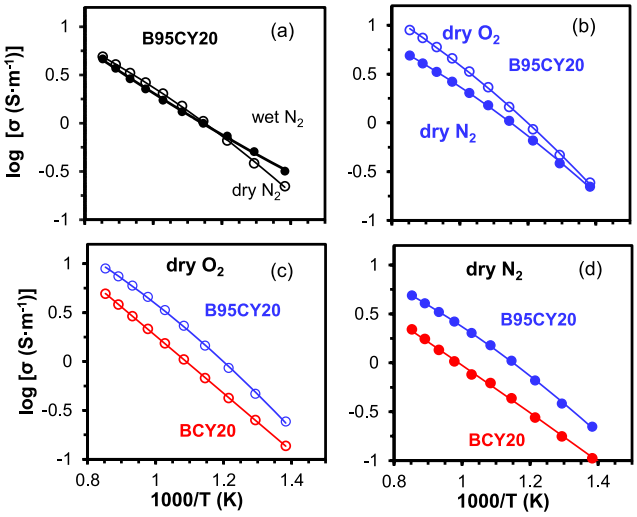

Fig. 4. Arrhenius plots of total conductivity for (a) B95CY20 in wet and dry N_2, (b) B95CY20 in dry O_2 and dry N_2, (c) BCY20 and B95CY20 in dry O_2 and (d) BCY20 and B95CY20 in dry N_2.

atmospheres in the low temperature interval indicates that proton transport is dominant. It is generally the case that perovskite proton conductors dehydrate at high temperature (>700 °C), with greater contributions from electron holes and oxide ions due to the exothermic nature of the hydration reaction eq. (1).

Fig. 4(b) shows the Arrhenius dependence of total conductivity in dry oxygen and nitrogen for B95CY20. At higher temperature, greater conductivity is exhibited in more oxidising dry conditions, attributable to an important contribution from electron holes, as occurs for BCY20 [15], according to the defect equilibrium:

$$v_O^{\cdot\cdot} + {}^1/_2 O_2 \overset{K_h}{\leftrightarrow} O_O^x + 2h^{\cdot}; \quad K_h \approx \frac{[h^{\cdot}]^2}{[v_o^{\cdot\cdot}]\, pO_2{}^{1/2}} \tag{6}$$

The convergence towards more similar conductivities at lower temperature has been observed for $BaZr_{0.7}Ce_{0.2}Y_{0.1}O_{3-\delta}$ (BZCY72) [32] and BCY20 [15] and is likely to be attributable to a decrease of the electron-hole contribution and a higher predominance of oxide ions, in dry conditions. In this regard, the higher activation energy of electron holes in comparison to oxide ions suggests that the contribution to total conductivity from the latter species is greater at lower temperature. Higher conductivities are observed for the Ba-deficient phase in comparison to the Ba-stoichiometric analogue in both dry O_2 and N_2 (Fig. 4 (c) and (d)), suggesting both a greater electron-hole and oxide-ion contribution in B95CY20, with a lesser influence of electron holes expected in the more reducing conditions. A more detailed investigation of the different contributions leading to the higher conductivities of Ba95CY20 is presented below.

3.4. Partial conductivities of electrical-transport species

The partial components of electrical conductivity were determined following a procedure developed by Frade [33] and Baek [34] and recently employed for barium-cerate based phases [15,35]. The methodology is focused on the defect equilibria and the expected effect that pO_2 and pH_2O exert on the different transport species.

On analysis of the defect equilibria for hydration and oxidation (eq. (1) and (6)), and considering that the oxygen vacancies are externally induced by Y-doping and Ba-deficiency (eq. (2)), the concentration of the different charge carriers may be expressed as [33–35]:

$$[OH_O^{\cdot}] \approx \frac{K_w pH_2O}{4}\left[\left(1+\frac{8\left([Y_{Ce}^{'}]+2[v_{Ba}^{''}]\right)}{K_w pH_2O}\right)^{1/2}-1\right] \tag{7}$$

$$[v_O^{\cdot\cdot}] \approx \frac{K_w pH_2O}{16}\left[\left(1+\frac{8\left([Y_{Ce}^{'}]+2[v_{Ba}^{''}]\right)}{K_w pH_2O}\right)^{1/2}-1\right]^2 \tag{8}$$

$$[h^{\cdot}] \approx \left(\frac{K_h K_w}{16}\right)^{1/2} pH_2O^{1/2} pO_2{}^{1/4}\left[\left(1+\frac{8\left([Y_{Ce}^{'}]+2[v_{Ba}^{''}]\right)}{K_w pH_2O}\right)^{1/2}-1\right] \tag{9}$$

where the following approximation has been employed for the electroneutrality condition, considering that the electron-hole concentration must be low in comparison to oxygen vacancies and protonic species, as is usually assumed [33]:

$$[Y_{Ce}^{'}]+2[v_{Ba}^{''}] \approx [OH_o^{\cdot}]+2[v_o^{\cdot\cdot}] \tag{10}$$

Grouping of some constants from eqs. (7)–(9) gives rise to the parameter α, defined as:

$$\alpha \approx \frac{8\left([Y_{Ce}^{'}]+2[v_{Ba}^{''}]\right)}{K_w} \tag{11}$$

Given that the partial conductivity of each charge carrier is the product of concentration, charge and mobility, the following expressions are obtained [35]:

$$\sigma_H = \sigma_H^0 \cdot \left[\left(1+\frac{\alpha}{pH_2O}\right)^{1/2}-1\right]\cdot\frac{pH_2O}{(1+\alpha)^{1/2}-1} \tag{12}$$

$$\sigma_O = \sigma_O^0 \cdot \left[\left(1+\frac{\alpha}{pH_2O}\right)^{1/2}-1\right]^2\cdot\frac{pH_2O}{\alpha} \tag{13}$$

$$\sigma_p = \sigma_p^0 \cdot \left[\left(1+\frac{\alpha}{pH_2O}\right)^{1/2}-1\right]\cdot\frac{pH_2O^{1/2}}{\alpha^{1/2}}\cdot pO_2{}^{1/4} \tag{14}$$

where σ_H^0, σ_O^0 and σ_p^0 are constants which correspond to the proton conductivity when $pH_2O = 1$ atm, the oxide-ion conductivity when $pH_2O = 0$ atm and the electron-hole conductivity when $pH_2O = 0$ atm and $pO_2 = 1$ atm, respectively.

According to eqs. (12)-(14) total conductivity, which is the sum of the partial components, may be expressed as follows:

$$\sigma_T = \sigma_H^0 \cdot \left[\left(1+\frac{\alpha}{pH_2O}\right)^{1/2}-1\right]\cdot\frac{pH_2O}{(1+\alpha)^{1/2}-1} + \sigma_O^0 \cdot \left[\left(1+\frac{\alpha}{pH_2O}\right)^{1/2}-1\right]^2\cdot\frac{pH_2O}{\alpha} + \sigma_p^0 \cdot \left[\left(1+\frac{\alpha}{pH_2O}\right)^{1/2}-1\right]\cdot\frac{pH_2O^{1/2}}{\alpha^{1/2}}\cdot pO_2{}^{1/4} \tag{15}$$

Under the condition of invariant pH_2O, eq. (15) may be simplified as:

$$\sigma_T = a + b\cdot pO_2^{1/4} \tag{16}$$

where a and b are constants, for a given condition of pH_2O, which take the form

$$a=\sigma_H^0\cdot\left[\left(1+\frac{\alpha}{pH_2O}\right)^{1/2}-1\right]\cdot\frac{pH_2O}{(1+\alpha)^{1/2}-1}+\sigma_O^0\cdot\left[\left(1+\frac{\alpha}{pH_2O}\right)^{1/2}-1\right]^2\cdot\frac{pH_2O}{\alpha} \quad (17)$$

and

$$b=\sigma_p^0\cdot\left[\left(1+\frac{\alpha}{pH_2O}\right)^{1/2}-1\right]\cdot\frac{pH_2O^{1/2}}{\alpha^{1/2}} \quad (18)$$

In the experimental methodology, for determination of partial components of conductivity, the total conductivity is measured as a function of $pO_2^{1/4}$ at a fixed degree of humidification.

Fitting the experimental results to the linear expression of eq. (16) at two different values of pH_2O and fixed temperature, gives rise to a system of four equations (Eq. (17) and (18)) with four unknown parameters, σ_H^0, σ_O^0, σ_p^0 and α, which may be determined by the corresponding analytical solution; in turn, the partial conductivities of each species may be determined (eqs. (12)-(14)).

The pO_2 dependencies of conductivity of Ba95CY20 at two different levels of humidification ($pH_2O \approx 2.2{\cdot}10^{-2}$ and $\approx 1.2{\cdot}10^{-3}$atm) are shown in Fig. 5 (a) and (b), together with a plot, Fig. 5 (c), of the dependence of conductivity with $pO_2^{1/4}$ at the different pH_2O values, following the linear relationship expected from the defect equilibria (eq. (16)). The solid lines which correspond to fitting of the experimental data according to the expected relationships provide a good fit, which is apparent in both the linear (Fig. 5(c)) and logarithmic representations (Fig. 5(a) and (b)). The slopes of the linear relations exhibited in Fig. 5 (c) increase with both increasing temperature and a lower level of humidification, indicating that both conditions lead to a greater electron-hole contribution to transport. It is apparent from the different intercepts of the slopes with different levels of humidification, corresponding to the total ionic conductivity, that the proportions of oxide-ionic and protonic species are temperature dependent.

The constant α was also used to determine the hydration equilibrium constant, eq. (11), the values of which at different temperatures exhibit Arrhenius–type behaviour with the inverse of temperature (Fig. 5(d)). A temperature-independent hydration enthalpy of −128 kJ mol^{-1} is obtained, within the range of values reported for parent compositions, and

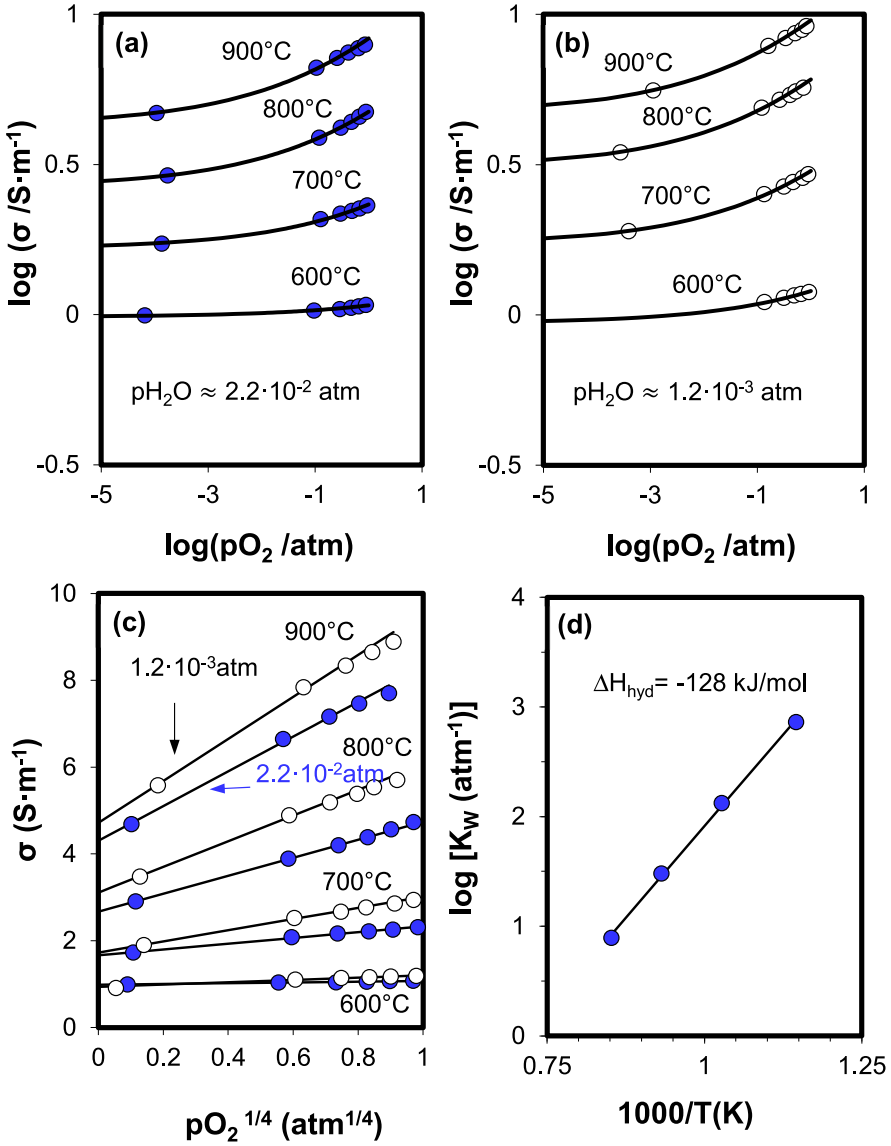

Fig. 5. Logarithmic representation of conductivity as a function of pO_2 for B95CY20 at (a) $pH_2O = 0.022$ atm and (b) $pH_2O = 0.0012$ atm; linear dependence of conductivity with $(pO_2)^{1/4}$ for B95CY20 at $pH_2O = 0.022$ and 0.0012 atm (c), and temperature dependence of the hydration equilibrium constant for B95CY20 (d).

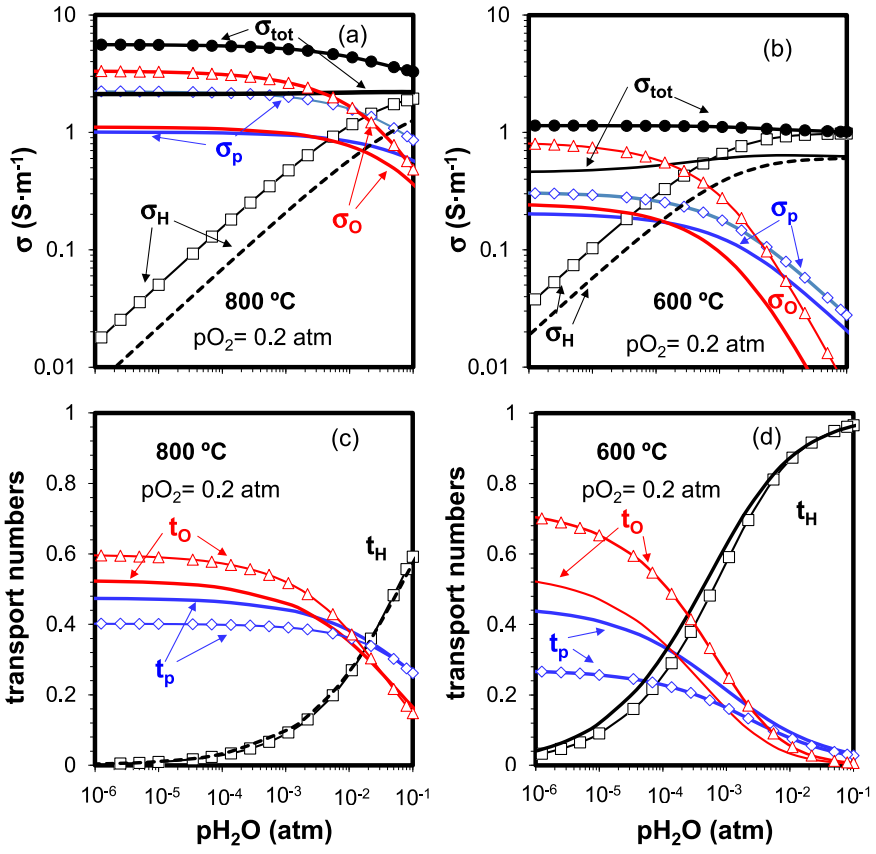

Fig. 6. Representation of: (a,b) total conductivity and partial conductivities and (c,d) transport numbers, associated to protons, oxide ions and holes as a function of water-vapour partial pressure in air at 800 °C (a,c) and 600 °C (b,d) for B95CY20 (symbols) and BCY20 (lines without symbols).

very similar to that reported for $BaCe_{0.9}Y_{0.1}O_{3-\delta}$ of −123 kJmol^{-1} [9].

The total electrical conductivity and its partial components as a function of pH_2O calculated on the basis of the relations given in eqs. (12)-(14), employing the constants σ_H^0, σ_O^0, σ_p^0 and α obtained by linear fittings, are shown in Fig. 6(a) and (b) at 800 and 600 °C for $pO_2 = 0.2$ atm. Firstly, we can see that at the higher temperature of 800 °C (Fig. 6 (a)), the conductivity decreases slightly when moving from dry to wet conditions, as was previously observed in Fig. 4(a). At this temperature, the conductivity is completely dominated by oxide ions and electron holes in dry conditions, and evolves towards triple-conducting behaviour in wet (Fig. 6(a)), with a protonic transport number of ≈0.36 at $pH_2O \approx 0.022$ atm (Fig. 6(c)). Moreover, as the temperature decreases to 600 °C (Fig. 6(b)), the electron-hole contribution in dry decreases to a greater extent than does the oxide-ion contribution. This is reflected in the corresponding transport numbers (Fig. 6(c) and (d)) which show that, in dry conditions, the electron-hole transport number is of greater influence at high temperature. As expected, the region in which the proton contribution is dominant is displaced to lower pH_2O in the lower temperature range (Fig. 6(b) and (d)). At 600, °C for wetter conditions (≥0.022 atm), the proton conductivity approaches that of the total conductivity and, consequently, protonic transport numbers higher than 0.92 are reached.

Although there are differences between the results of BCY20 and B95CY20, both materials behave similarly as a function of pO_2, pH_2O and temperature, as expected from their similar composition and structure. Nevertheless, the contribution of each species is higher for the Ba-deficient sample, leading, in turn, to a higher total conductivity. In dry conditions, both phases are principally mixed conductors of electron holes and oxide-ion vacancies. In this region, proton transport increases with a $(pH_2O)^{1/2}$ power law, in accordance with the expected defect-chemistry equilibria at the dilute limit for protonic charge carriers [36]. For higher levels of humidification, proton transport becomes predominant at the expense of diminishing electron-hole and oxide-ion contributions. The higher protonic conductivity of B95CY20 compared to BCY20 is apparent at 600 °C for typical values of $pO_2 = 0.2$ atm and $pH_2O = 0.022$ atm, where the total conductivity is mainly protonic for both compositions ($t_H = 0.92$, Fig. 6(d)), reaching respective values of 1.04 and 0.63 S m^{-1}.

Fig. 7 shows the temperature dependence of total and partial conductivities ((a) and (b)) and electrical transport numbers ((c) and (d)), for B95CY20 at $pO_2 = 1$ ((a) and (c)) and 10^{-4} atm ((b) and (d)), under typical wet conditions of $pH_2O = 0.022$ atm. At 600 °C, transport is principally protonic in both oxidising and reducing conditions (Fig. 7(a) and (b)), with a greater protonic transport number in reducing ($t_H = 0.96$, Fig. 7(d)) in comparison to oxidising conditions ($t_H = 0.89$, Fig. 7 (c)). The electron-hole conductivity is more influential in oxidising atmospheres, and is the principal contributor to the electrical transport at 900 °C in O_2, with a transport number of $t_p = 0.48$ (Fig. 7(c)). This value decreases to 0.08 when pO_2 lowers to 10^{-4} atm at 900 °C (Fig. 7(d)) and goes down continuously with decreasing temperature, becoming practically negligible at 600 °C. The dependencies of the electrical behaviour under simultaneous influences of pO_2, pH_2O and temperature are exhibited in a 3D representation of the electrical transport of B95CY20 as a function of pO_2 and pH_2O in the range 600–900 °C, Fig. 8.

4. Discussion

The introduction of A-site deficiency is a well-known strategy for

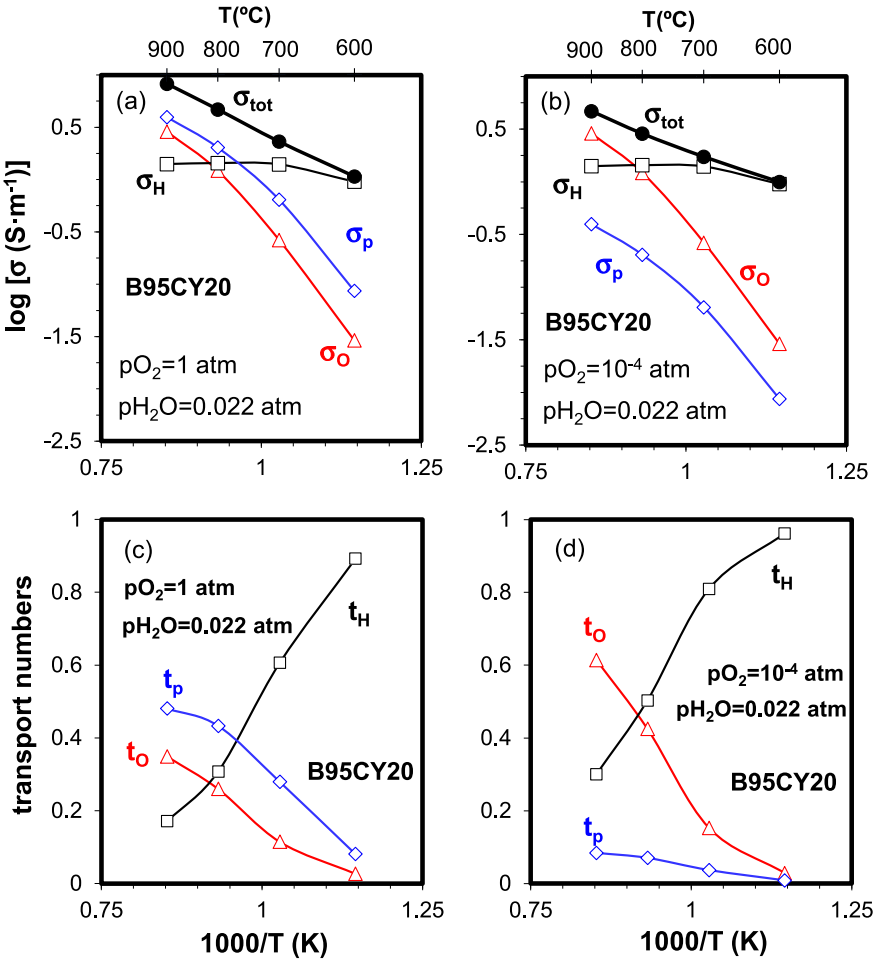

Fig. 7. Representation of total and partial components of conductivity (a)–(b) and transport numbers (c)–(d) as a function of temperature for B95CY20, in wet conditions (pH_2O = 0.022 atm), for pO_2 = 1 atm (a)–(c) and 10^{-4} atm (b)–(d).

lowering the chemical potential of the basic A-site cation species in perovskite oxides and improving stability towards carbonation or hydration. Nevertheless, there are only a handful of studies of the effects of Ba deficiency in proton-conducting barium cerates despite its widely known poor stability [30]. As mentioned, improvement in stability with Ba deficiency has also recently been associated with removal of an amorphous, resistive nanolayer of BaO in the case of $BaCe_{1-x}M_xO_{3-\delta}$ (M = Dy, Gd, Sm, Y) [16]. This report highlights the amelioration of grain-boundary conductivity with Ba substoichiometry, which occurs in the lower temperature range, 400–700 °C.

In general, the effect of A-site deficiency on the defect chemistry and, in turn, electrical properties of proton-conducting perovskites paints a rather complex picture. Sr deficiency in the $SrCe_{0.9}Yb_{0.1}O_{3-\delta}$ system is compensated by A-site vacancy formation for low Sr vacancy contents but, at higher levels, dopant-cation occupancy of the A site occurs (dopant partitioning, eq. (3)), leading to anomalous variation of lattice parameters with increasing A-site vacancy concentration [37]. Shima and Haile consider unit-cell volumes to indicate that the Gd dopant occupies the A site in the system $Ba_{1-x}Ce_{0.9}Gd_{0.1}O_{3-\delta}$ [38]. The conductivity decreases with decreasing Ba content consistent with the consumption of oxygen vacancies in accordance with eq. (2). Other work by Jaiswal et al. [17] again shows both lower conductivity and lattice parameter with increasing Ba deficiency, this time for the system $(Ba_{0.6-p}Sr_{0.4})(Ce_{0.75}Zr_{0.1}Y_{0.15})O_{3-\delta}$, and confirms improved stability against CO_2. In contrast, the results of Wu et al. [39] of the $Ba_{1-x}Ce_{0.8}Sm_{0.2}O_{3-\delta}$ system are similar to those of $Sr_{1-x}Ce_{0.9}Yb_{0.1}O_{3-\delta}$ [37] with conductivity passing through a maximum with increasing nominal A-site deficiency.

Here, our detailed analysis of partial electrical components of B95CY20 in the temperature range 600–900 °C shows enhanced conductivity in a wide range of pH_2O atmospheres in comparison to BCY20 (Fig. 6). This enhancement is, *a priori*, attributable to a greater concentration of positive charge carriers introduced via the vacancy mechanism (eq. (2), oxide-ion vacancy formation), with subsequent hydration (eq. (1), proton formation) or oxidation (eq. (6), electron-hole formation). Supporting this hypothesis is the fact that the A-O bond length is slightly longer and specific free volume [40,41] slightly greater in B95CY20 than for BCY20 synthesized under the same conditions (Ba95CY20: 3.124 Å and 0.842; BCY20: 3.118 Å and 0.838). Otherwise, it would be expected that dopant partitioning of the smaller Y^{3+} cation on the A site would lead to a decrease in unit-cell volume as described for other systems [37,38,42]. In this respect, the present conductivity results correlate well with those of the $Sr_{1-x}Ce_{0.9}Yb_{0.1}O_{3-\delta}$ system, in which greater conductivity is also matched by a greater specific free volume [37].

It is clear, nevertheless, that the dominant compensation mechanism for deficiency of the A-site cation and resultant electrical properties depend to a significant extent on the degree of deficiency, dopant content and ionic radius, and related structural and compositional factors. It cannot be assumed that a particular behaviour may be extrapolated across a range of dopants within a particular system. In the case of BCY20, a greater proportion of A-site (and oxygen) vacancies may be generated in comparison to Gd- and Sm-doped $BaCeO_3$ systems [38,39] due to ionic-radii considerations, namely the larger Gd^{3+} and Sm^{3+}

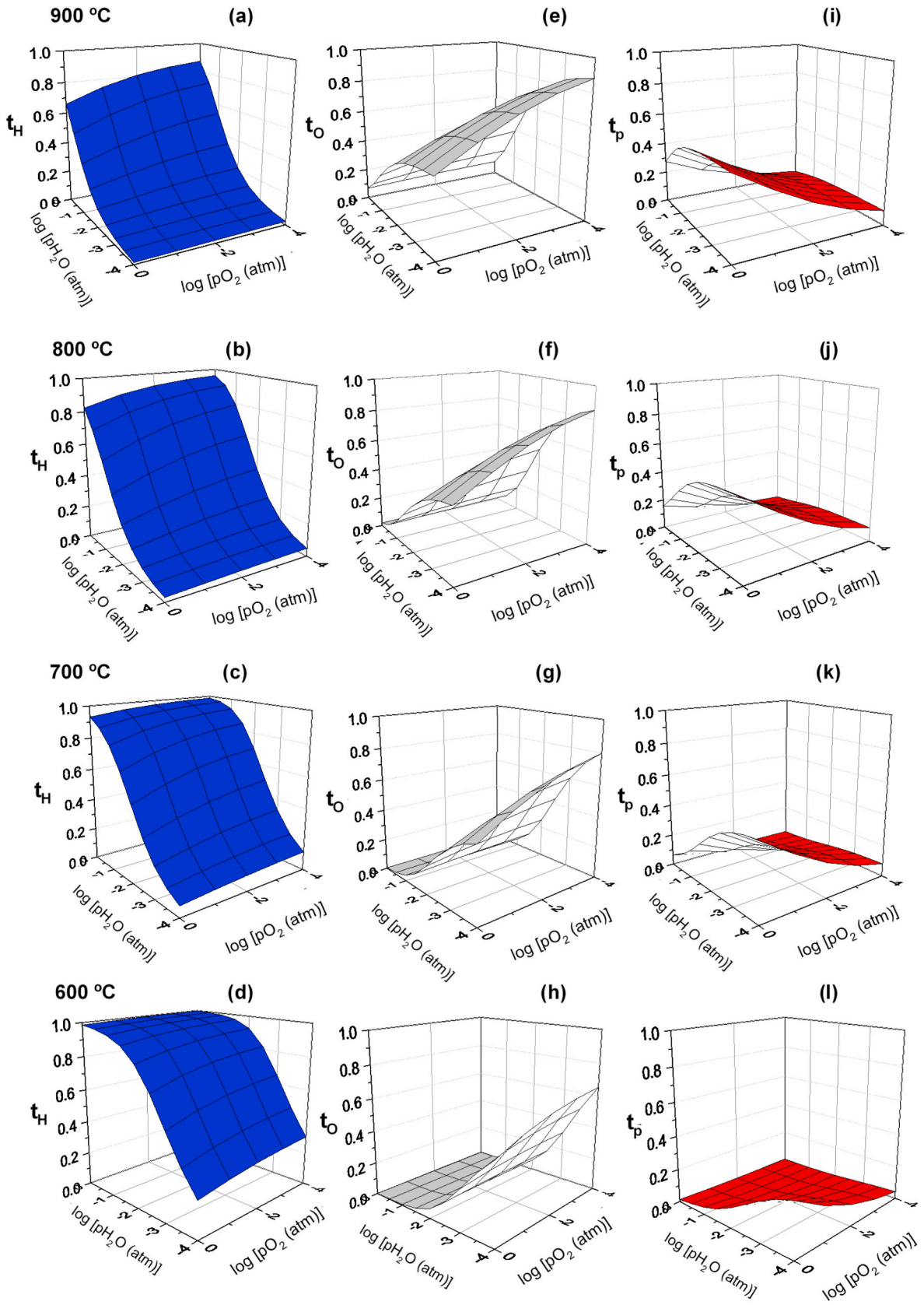

Fig. 8. Protonic (a–d), oxide-ionic (e–h) and electron-hole (i–l) transport numbers as functions of pO_2 and pH_2O in the range 600–900 °C.

cations ($^{VIII}r = 1.053$ and 1.079 Å, respectively [43]) may be more easily accommodated on the Ba site than the smaller Y^{3+} cation ($^{VIII}r = 1.019$ Å).

Finally, we should point out that the Ba-deficient B95CY20 phase shares a number of characteristics with Br-synthesized BCY20 which we recently studied [15]. Both materials show an improvement of total electrical conductivity attributable to dominant positive charge carriers, the concentrations of which are dependent on the prevalent atmosphere and temperature. The two materials also exhibit both greater cell volume and monoclinic distortion than BCY20, the former phenomenon suggesting formation of the positive charge carriers through an A-site vacancy mechanism, as discussed above. This supports our earlier hypothesis that Ba substoichiometry of the main phase in Br-synthesized BCY20 explains the behavioural differences with BCY20. One area in which the Ba-deficient and Br-synthesized materials show different behaviour is the improvement in stability towards carbonation in the former and the opposing effect in the latter. This seems to indicate that the Ba excess in the Br-synthesized phase resides in the grain boundaries thereby lowering stability.

5. Conclusions

The effects of Ba deficiency on stability, structure and electrical properties have been studied for the proton-conducting $Ba_{0.95}Ce_{0.8}Y_{0.2}O_{3-\delta}$ perovskite. Rietveld refinement of neutron powder diffraction data indicates that the Ba substoichiometric phase crystallizes with a monoclinic distortion of the perovskite structure at room temperature (space group, *I2/m*). XRD and confocal Raman microscopy integrated with atomic force microscopy of samples exposed to laboratory air over a prolonged period confirm previous reports of improved resistance to carbonation of the Ba-deficient material in comparison to the nominally Ba-stoichiometric analogue.

Electrical-conductivity measurements under different conditions of oxygen and water-vapour partial pressures were employed to determine the influence of protonic, oxide-ionic and electronic charge carriers in the temperature range 600–900 °C on analysis with a defect-chemistry-based method. Total conductivity is considerably higher in the Ba-deficient material in comparison to the Ba-stoichiometric phase. The increase in transport in dry oxidising conditions is attributable to greater mixed oxide-ionic-electron-hole contribution, whereas in wet conditions and lower temperature the higher conductivity is due to greater proton transport. The enhanced conductivity may be credited to a greater number of charge carriers in the Ba-stoichiometric phase, although structure-related features such as a higher specific free volume may also play a role.

The combined positive effects of both improved stability and electrical transport of Ba substoichiometry in one of the earliest discovered and best conducting high-temperature proton conductors is thus confirmed as an important strategy for reappraising the applicability of this material in a range of high-temperature electrochemical devices.

CRediT authorship contribution statement

Ángel Triviño-Peláez: Investigation, Methodology, Formal analysis, Writing – original draft. **Domingo Pérez-Coll:** Conceptualization, Formal analysis, Writing – review & editing, Project administration. **Jadra Mosa:** Conceptualization, Investigation, Supervision, Writing – original draft. **Clemens Ritter:** Investigation, Writing – review & editing. **Ulises Amador:** Validation, Investigation, Writing – review & editing. **Glenn C. Mather:** Conceptualization, Writing – review & editing, Supervision, Project administration, Funding acquisition.

Declaration of competing interest

The authors declare that they have no known competing financial interests or personal relationships that could have appeared to influence the work reported in this paper.

Acknowledgements

We thank MICINN (Spain) for financial assistance through the predoctoral grant BES-2016-077023 and projects RTI2018-095088-B-I00, RTI2018-09573-J-I00 and MAT2017-90695-REDT. Access to the neutron facilities at the Institut Laue Langevin (Grenoble, France) is gratefully acknowledged (proposal EASY-459; DOI: 10.5291/ILL-DATA.EASY-459).

Appendix A. Supplementary data

Supplementary data to this article can be found online at https://doi.org/10.1016/j.jpowsour.2021.229691.

References

[1] H. Matsumoto, S. Okada, S. Hashimoto, K. Sasaki, R. Yamamoto, M. Enoki, T. Ishihara, Ionics (Kiel). 13 (2007) 93.
[2] I. Hiroyasu, Solid State Ionics 77 (1995) 289.
[3] E. Fabbri, L. Bi, D. Pergolesi, E. Traversa, Adv. Mater. 24 (2012) 195.
[4] T. Sakai, S. Matsushita, H. Matsumoto, S. Okada, S. Hashimoto, T. Ishihara, Int. J. Hydrogen Energy 34 (2009) 56.
[5] K. Kreuer, Solid State Ionics 97 (1997) 1.
[6] K.D. Kreuer, Solid State Ionics 125 (1999) 285.
[7] C.W. Tanner, A. V Virkar, J. Electrochem. Soc. 143 (1996) 1386.
[8] S. Robinson, A. Manerbino, W. Grover Coors, N.P. Sullivan, Fuel Cell. 13 (2013) 584.
[9] S. Ricote, N. Bonanos, G. Caboche, Solid State Ionics 180 (2009) 990.
[10] N. Nasani, P.A.N. Dias, J.A. Saraiva, D.P. Fagg, Int. J. Hydrogen Energy 38 (2013) 8461.
[11] N. Tarasova, I. Animitsa, Solid State Ionics 317 (2018) 21.
[12] Y. Wang, H. Wang, T. Liu, F. Chen, C. Xia, Electrochem. Commun. 28 (2013) 87.
[13] H. Zhou, L. Dai, L. Jia, J. Zhu, Y. Li, L. Wang, Int. J. Hydrogen Energy 40 (2015) 8980.
[14] K. Belova, S. Baskakova, C. Argirusis, I. Animitsa, Electrochim. Acta 193 (2016) 63.
[15] Á. Triviño-Peláez, D. Pérez-Coll, G.C. Mather, Acta Mater. 167 (2019) 12.
[16] H.S. Kim, H. Bin Bae, W.C. Jung, S.Y. Chung, Nano Lett. 18 (2018) 1110.
[17] S.M. Choi, J.-W. Son, H.-W. Lee, J.-H. Lee, S.K. Jaiswal, K.J. Yoon, B.-K. Kim, Int. J. Hydrogen Energy 40 (2015) 11022.
[18] C. Zhang, H. Zhao, Mater. Res. Bull. 45 (2010) 1659.
[19] J. Rodriguez-Carvajal, Phys. B 192 (1993) 55.
[20] H.-D. Baek, Solid State Ionics 110 (1998) 255.
[21] J.T.S. Irvine, D.C. Sinclair, A.R. West, Adv. Mater. 2 (1990) 132.
[22] L. Malavasi, C. Ritter, G. Chiodelli, Chem. Mater. 20 (2008) 2343.
[23] G.C. Mather, G. Heras-Juaristi, C. Ritter, R.O. Fuentes, A.L. Chinelatto, D. Pérez-Coll, U. Amador, Chem. Mater. 28 (2016) 4292.
[24] L.B. McCusker, R.B. Von Dreele, D.E. Cox, D. Louër, P. Scardi, J. Appl. Crystallogr. 32 (1999) 36.
[25] C.S. Transactions, J.M. Sailaja, K.V. Babu, N. Murali, K. Samatha, V. Veeraiah, A. Pradesh, Chem. Sci. Trans. 5 (2016) 687.
[26] S. Nieto, R. Roque-Malherbe, R. Polanco, L. Fuentes-Cobas, R.S. Katiyar, Ceram. Int. 40 (2014) 11359.
[27] T. Scherban, R. Villeneuve, L. Abello, G. Lucazeau, Solid State Commun. 84 (1992) 341.
[28] T. Scherban, R. Villeneuve, L. Abello, G. Lucazeau, Solid State Ionics 61 (1993) 93.
[29] I. Charrier-Cougolic, T. Pagnier, G. Lucazeau, J. Solid State Chem. 227 (1999) 220.
[30] M. Scholten, J. Schoonman, J. Vanmiltenburg, H. Oonk, Solid State Ionics 61 (1993) 83.
[31] I. Antunes, G.C. Mather, J.R. Frade, J. Gracio, D.P. Fagg, J. Solid State Chem. 183 (2010) 2826.
[32] G. Heras-Juaristi, U. Amador, R.O. Fuentes, A.L. Chinelatto, J. Romero De Paz, C. Ritter, D.P. Fagg, D. Pérez-Coll, G.C. Mather, J. Mater. Chem. 6 (2018) 5324.
[33] J.R. Frade, Solid State Ionics 78 (1995) 87.
[34] H.-D. Baek, Solid State Ionics 110 (1998) 255.
[35] G. Heras-Juaristi, D. Pérez-Coll, G.C. Mather, J. Power Sources 364 (2017) 52.
[36] S.-J. Song, E.D. Wachsman, S.E. Dorris, U. Balachandran, J. Electrochem. Soc. 150 (2003) A1484.
[37] G.C. Mather, S. García-Martín, D. Benne, C. Ritter, U. Amador, J. Mater. Chem. 21 (2011) 5764.
[38] D. Shima, S.M. Haile, Solid State Ionics 97 (1997) 443.
[39] X. Wu, H. Wang, R. Peng, C. Xia, G. Meng, Solid State Ionics 192 (2011) 611.
[40] A.F. Sammells, R.L. Cook, J.H. White, J.J. Osborne, R.C. MacDuff, Solid State Ionics 52 (1992) 111.
[41] H. Hayashi, H. Inaba, M. Matsuyama, N.G. Lan, M. Dokiya, H. Tagawa, Solid State Ionics 122 (1999) 1.
[42] S.K. Jaiswal, S.M. Choi, K.J. Yoon, J.W. Son, B.K. Kim, H.W. Lee, J.H. Lee, Int. J. Hydrogen Energy 40 (2015) 11022.
[43] R.D. Shannon, Acta Crystallogr. A 32 (1976) 751.